Supplementary Material
Moiré tuning of spin excitations: Individual Fe atoms on MoS_2/Au(111)

Sergey Trishin,[1] Christian Lotze,[1] Nils Bogdanoff,[1] Felix von Oppen,[2] and Katharina J. Franke[1]

[1] *Fachbereich Physik, Freie Universität Berlin, 14195 Berlin, Germany*

[2] *Dahlem Center for Complex Quantum Systems and Fachbereich Physik, Freie Universität Berlin, 14195 Berlin, Germany*

S1. ELECTRONIC MOIRÉ MODULATION

In the main text we show that magnetic excitations of individual Fe atoms strongly depend on their adsorption site with respect to the moiré structure. The moiré structure is a result of a lattice mismatch of the MoS_2 and Au(111) lattices, which leads to modulations of the atomic stacking order at the interface with a periodicity of 3.3 nm. The moiré structure is immediately reflected in STM images (Fig. S1a), which are a convolution of topographic and electronic structure. Simultaneously recorded atomic force microscopy images revealed small variations in topographic height, coexisting with a sizable electronic modulation [1]. The latter is expressed in $\mathrm{d}I/\mathrm{d}V$ spectra of the valence and conduction band of MoS_2 on Au(111) (Fig. S1b). The spectrum taken on a maximum of the moiré structure shows a shoulder at $V =\sim -2.0\,\mathrm{V}$, which is associated to states at $\bar{Q}$ in the Brillouin zone and appears shifted by $\sim 300\,\mathrm{mV}$ toward the Fermi level at the moiré minimum. In contrast, the most pronounced peaks of the conduction band at $V \simeq 0.9\,\mathrm{V}$ and $V \simeq 1.4\,\mathrm{V}$, which are attributed to bands at the $\bar{\Gamma}$ point, are shifted by $\sim 60\,\mathrm{mV}$ toward the Fermi level on the moiré maximum. We note that we cannot resolve states with large in-plane ($k_\parallel$) component, such as the valence band maximum and conduction band minimum in STS, because the tunneling current is mainly carried by electrons with small $k_\parallel$ component. Hence, STS is not sensitive to states at $\bar{K}$, which dominate the band onsets and, hence, the states closest to the Fermi level. We suggest that the modulated conduction band is responsible for the modulation of the density of states at the Fermi level and, hence, the modulation of the effective exchange coupling $J\rho$ of the Fe atoms shown in the main manuscript.

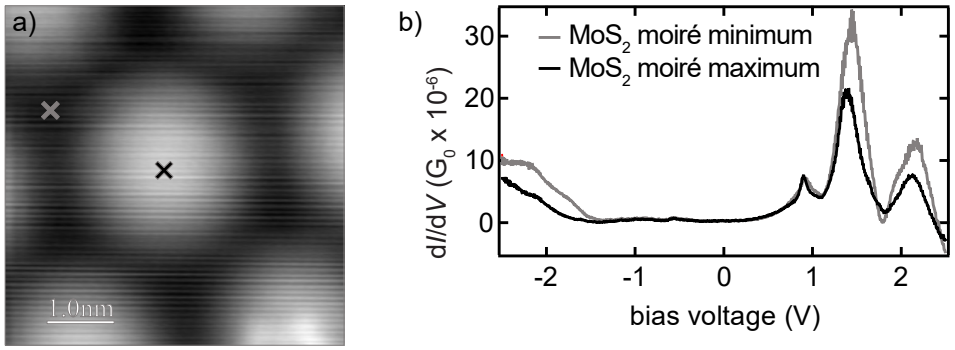

Figure S1. (a) STM topography of a clean MoS_2 island, showing the moiré structure. Image recorded at $V = 50\,\mathrm{mV}$, $I = 100\,\mathrm{pA}$. (b) Differential conductance spectra recorded on the maximum and minimum of the moiré structure. Spectra taken after opening the current feedback at a setpoint of $V = 10\,\mathrm{mV}$, $I = 20\,\mathrm{pA}$ with an additional retraction of the tip by 220 pm, lock-in frequency $f = 911\,\mathrm{Hz}$, lock-in modulation $V_{\mathrm{rms}} = 5\,\mathrm{mV}$.

S2. IDENTIFICATION OF FE ADATOMS ON DEFECTS

As described in the main manuscript, the majority of Fe atoms are imaged as triangularly-shaped protrusions at low bias voltage. In contrast, a minority of protrusions is of circular shape (Fig. S2a). A clear distinction between the triangular and circularly-shaped Fe atoms can also be found in their differential conductance spectra in a larger energy range (Fig. S2b). The triangular-appearing atoms exhibit states above 0.5 V, but no states within the occupied region. This is in contrast to the findings on the circularly-shaped Fe atoms, which show substantial conductance in

a broad energy range below -0.2 V. We also observe a narrow peak at zero bias, which may be associated to a Kondo resonance.

To unravel the origin of the different types of Fe atoms, we remove all Fe atoms by scanning at small tip-sample distance ($I = 25\,\mathrm{nA}$, $V = 50\,\mathrm{mV}$). The subsequently recorded STM image reveals several local defects (Fig. S3). By comparison with the previous STM image with the Fe atoms, we conclude that the circularly-shaped Fe atoms had been located on defects. While we have shown an example of one Fe atom on a defect site in Fig. S2b, we remark that Fe atoms on different defects showed a large variety of $\mathrm{d}I/\mathrm{d}V$ features which we do not consider further in this paper.

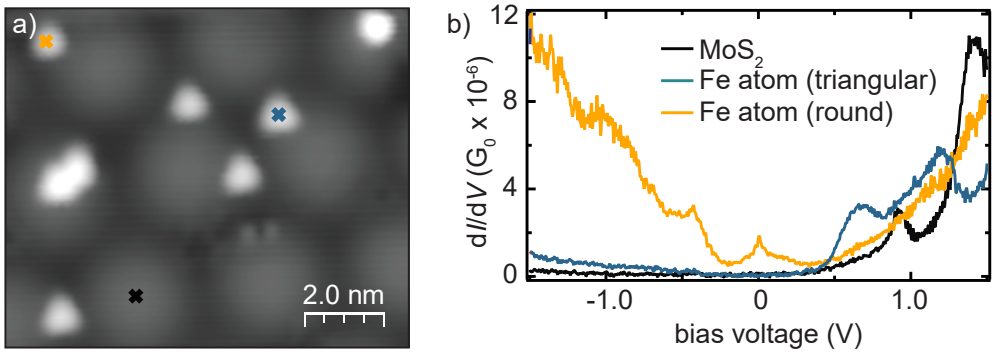

Figure S2. (a) Close-up view of Fe atoms adsorbed on a MoS_2 island. The moiré structure is seen in the background. The Fe atoms appear either triangular or circular shaped. Image recorded at $V = 50\,\mathrm{mV}$, $I = 100\,\mathrm{pA}$. (b) Differential conductance spectra recorded on a triangular (blue) and circular (orange) shaped Fe atom. The spectrum on MoS_2 (black) is shown for reference, revealing the well-known band gap with conduction band onset at 0.5 V and valence band onset at -1.4 V [1–3]. Spectra taken after opening the current feedback at a setpoint of $V = 1.5\,\mathrm{V}$, $I = 300\,\mathrm{pA}$, lock-in modulation $V_{\mathrm{rms}} = 5\,\mathrm{mV}$.

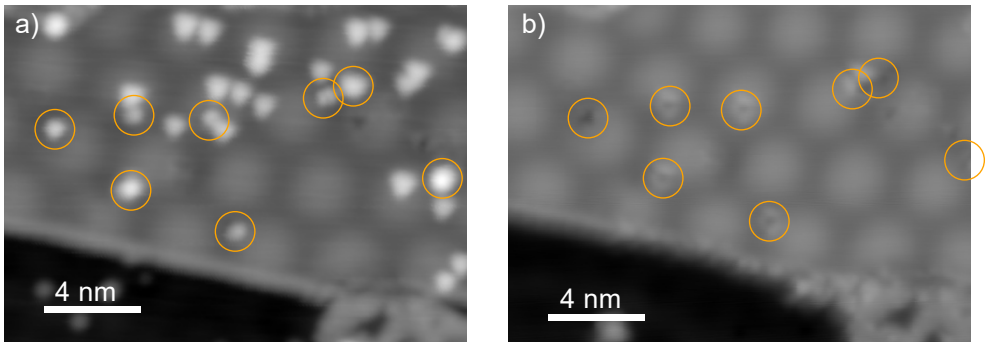

Figure S3. (a) STM topography image of an Fe-decorated MoS_2 island. The majority of the Fe atoms appears triangular shaped, while some atoms take on different shapes (marked by orange circles). (b) STM topography image of the same area as in (a) taken after removing all Fe atoms. This has been achieved by scanning at small bias voltage and large currents ($V = 4.7\,\mathrm{mV}$, $I = 25\,\mathrm{nA}$). The locations of the atoms which had been imaged with non-triangular shape are marked again by orange circles. Topographies were recorded at a setpoint of $V = 50\,\mathrm{mV}$, $I = 100\,\mathrm{pA}$.

S3. FITS TO SPECTRAL LINESHAPES AT DIFFERENT MOIRÉ SITES

In Fig. 2 of the main manuscript, we plotted the $\mathrm{d}I/\mathrm{d}V$ spectra recorded at the center above Fe atoms located at different sites with respect to the moiré structure. The lineshapes varied from purely symmetric steps around the Fermi level when the atom was located on a moiré minimum to an asymmetric peak, when the Fe atom was located at a moiré maximum. When moving from the minimum to the maximum, the lineshapes were more complex. To

understand the origin of lineshape variations we applied different fits to the dI/dV spectra. The fits were shown as black dashed lines in Fig. 2.

The spectrum in Fig. 2a can be reproduced by symmetric Fermi-Dirac functions located at 2.7 mV with a width of 0.45 meV (error of the fit $\chi^2 = 7.4 \times 10^{-8}$). The very good fit evidences that pure inelastic spin excitations dominate the dI/dV spectrum.

The spectra in Fig.2b-d exhibit additional cusps on top of the inelastic steps. These spectra are fitted within a perturbative approach in the exchange interaction [4]. Fit parameters were extracted to be: $J\rho = -0.11$, $U = -0.32$, $D = 2.5\,\mathrm{mV}$ ($\chi^2 = 3 \times 10^{-7}$) (b), $J\rho = -0.16$, $U = -0.71$, $D = 2.3\,\mathrm{mV}$ ($\chi^2 = 4 \times 10^{-7}$) (c) and $J\rho = -0.33$, $U = -1$, $D = 1.73\,\mathrm{mV}$ ($\chi^2 = 1.9 \times 10^{-6}$) (d). The model captures the lineshapes in Fig. 2b,c very well. The increase in density of states thus induces additional Kondo correlations, which can be treated perturbatively in the exchange coupling strength to the substrate. However, even the best fit parameters in Fig. 2d do not reproduce the lineshape. This indicates the limitation of the perturbative approach upon further increasing the strength of the exchange coupling.

When the atoms are located even further from the minimum, the dI/dV spectra take on lineshapes that deviate completely from the perturbative model. The spectrum in Fig.2e was fitted using a Frota lineshape with an additional Lorentz peak with fit parameters: Frota phase $\phi = 3.87$, Frota width $\Gamma = 2.21\,\mathrm{mV}$, Frota center $x_0 = 1.3\,\mathrm{mV}$, Lorentz width $\Gamma_L = 0.79\,\mathrm{mV}$ and Lorentz position $x_L = 0.11\,\mathrm{mV}$ ($\chi^2 = 1.5 \times 10^{-7}$). The presence of a Frota peak indicates strong exchange correlations, while the dip indicates inelastic spin excitations.

Finally, in Fig. 2f the spin excitation gap has closed, resulting in a fully developed Frota lineshape that can be reproduced by: $\phi = 4.12$, $\Gamma = 3.49\,\mathrm{mV}$, $x_0 = 1.6\,\mathrm{mV}$ ($\chi^2 = 9.1 \times 10^{-8}$).

S4. DETERMINATION OF THE POTENTIAL SCATTERING U AT AN FE ATOM CLOSE TO THE MOIRÉ MINIMUM

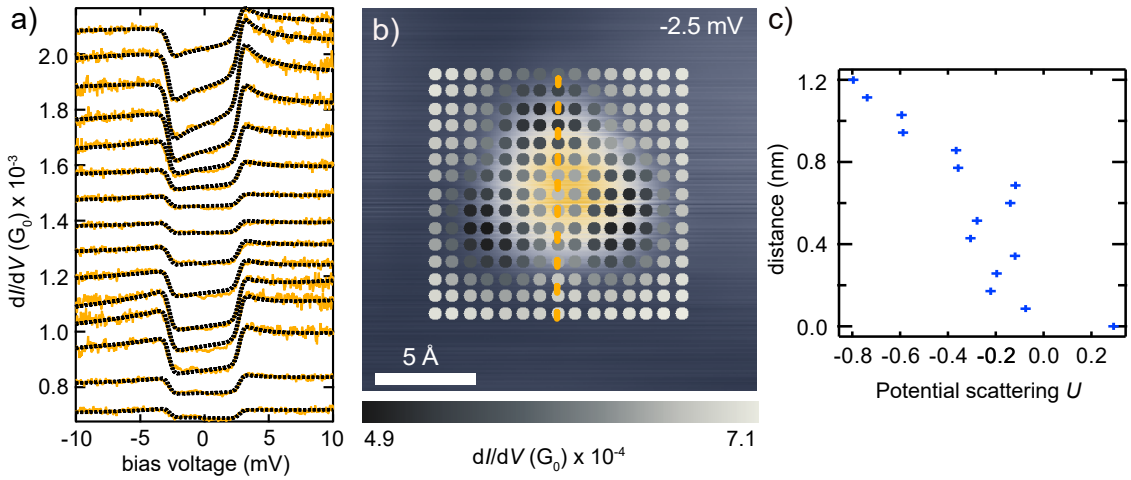

Figure S4. (a) Stacked plot of dI/dV spectra taken along the orange dashed line in (b), spectra are offset for clarity. Every second spectrum was also plotted in Fig. 3d of the main manuscript. (b) Differential conductance signal extracted from a densely-spaced grid of spectra across an Fe atom on the moiré minimum at $V = -2.5\,\mathrm{mV}$ (same as in Fig. 3e in the main text). (c) Extracted values for the potential scattering parameter U obtained by fits according to Ref. [4] with $J\rho = -0.132$ and $D = 2.75\,\mathrm{meV}$ kept constant (fits shown as black dashed lines in (a)). The spectra in (a) and (b) were recorded at a setpoint of $V = 10\,\mathrm{mV}$, $I = 1\,\mathrm{nA}$, with a lock-in modulation of $V_{\mathrm{rms}} = 50\,\mu\mathrm{V}$.

In the main manuscript we discussed the differences between spectra recorded on and in the immediate vicinity of the Fe atoms. When the Fe atoms sit on or close to the minima of the moiré structure, the dI/dV lineshapes can be fitted by calculating the conductance including inelastic electron scattering up to second order in Born approximation and potential scattering [4]. These fits allow for an evaluation of the variations in exchange and potential scattering strength. Here, we present a set of spectra taken along one of the high-symmetry axes of the Fe–S complex (spectra in Fig. S4a along dashed line in S4b). From the corresponding fits with fixed exchange coupling $J\rho$ we find that the

potential scattering U varies across the Fe–S complex (S4c). We observe the largest values of U at the triangle's vertex and a gradual decrease towards the center.

S5. LOCAL VARIATIONS OF LINESHAPES ON FE ATOMS CLOSE TO THE MOIRÉ MAXIMUM

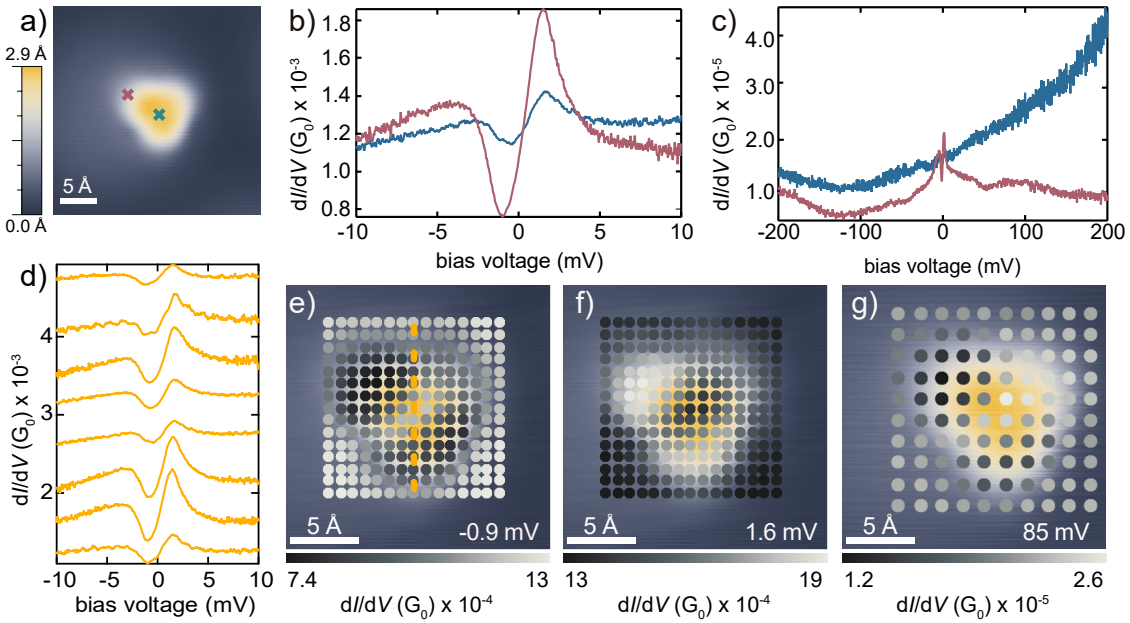

Figure S5. (a) STM topography image of an Fe atom close to a maximum of the moiré structure ($V = 10\,\mathrm{mV}$, $I = 1\,\mathrm{nA}$). (b,c) Differential conductance spectra on the center (blue cross) and vertex (purple cross) of triangular shape of the Fe adatoms. (d) Stacked plot of spectra (offset for clarity) along the orange dashed line indicated in (e). (e-g) STM topographies (blue-yellow, background) with superimposed differential conductance signal at the indicated bias voltage (black-white dots, scale given below panels) extracted from a densely spaced grid of spectra across the Fe atom at the indicated energies. The spectra in (b), (e) and (f) were recorded at a setpoint of $V = 10\,\mathrm{mV}$, $I = 1\,\mathrm{nA}$, the spectra in (c) and (g) at $V = 10\,\mathrm{mV}$, $I = 20\,\mathrm{pA}$, with an additional retraction of the tip by $z = 20\,\mathrm{pm}$. The lock-in frequency was $f = 911\,\mathrm{Hz}$, the lock-in modulation amplitude for (b), (e) and (f) was $V_{\mathrm{rms}} = 50\,\mu\mathrm{V}$, for (c) and (g) $V_{\mathrm{rms}} = 1\,\mathrm{mV}$.

In the main manuscript we investigated the spatial variations of spectra in the close vicinity of an Fe atom adsorbed on a minimum of the moiré structure. The reason for this choice was that the Fe atom was among the most weakly coupled to the substrate such that the excitations could be described within second-order perturbation theory, and the lineshape could be fitted by the code developed by Ternes [4]. In Fig. S5 we provide complementary data on an Fe atom adsorbed close to a maximum of the moiré structure. As explained in the main manuscript, the $\mathrm{d}I/\mathrm{d}V$ lineshape of the low-energy spectrum recorded on the center of the atom is highly asymmetric in bias voltage (blue spectrum in Fig. S5b). The lineshape at the vertex of the triangular shape is again different compared to the center (purple spectrum in Fig. S5b). The spectral variation along one of the (expected) threefold symmetry axes of the Fe–S complex is plotted in Fig. S5d. In addition, the spatial variations are mapped by plotting the $\mathrm{d}I/\mathrm{d}V$ signal at $-0.9\,\mathrm{mV}$ and $1.6\,\mathrm{mV}$ from a densely-spaced grid of $\mathrm{d}I/\mathrm{d}V$ spectra (Fig. S5e,f). Similar to the case of the Fe atoms on the moiré minima, the asymmetry is enhanced at the vertices of the Fe–S complex. However, the expected threefold symmetry of the Fe–S complex is broken by the superposition of the moiré modulation, which additionally contributes to the lineshape variations.

To probe the correlations of the low-energy variations with the higher-energy electronic structure, we plot the $\mathrm{d}I/\mathrm{d}V$ spectra over a larger energy range in Fig. S5c. On the Fe center, the spectrum consists of a broad slope, while a spectrum on a vertex shows a faint peak at $\sim 85\,\mathrm{mV}$. We extract its spatial intensity distribution from a densely-spaced grid of spectra (Fig. S5g). It reflects the same symmetry as the low-energy features in Fig. S5e,f, corroborating again the correlation between the orbital structure and the lineshape of inelastic excitations. Although we cannot fit these spectra to extract values of U, the asymmetry variations are in agreement with a variation of

potential scattering as quantified for Fe atoms on the moiré minimum. We thus suggest that the variations in spectral features can also be explained by the different contributions to the interfering tunneling paths.

S6. INTERFERENCE WITHIN A TWO-ORBITAL MODEL

Here, we briefly discuss the interference due to tunneling via two separate orbitals, following Ref. [5]. As discussed in the main text, we assume that tunneling proceeds via an orbital (or a set of orbitals) giving rise to the Fe spin as well as a second, possibly nonmagnetic hybrid orbital, which presumably underlies the resonance observed at a bias of order 150 meV. As usual, the magnetic orbitals are singly occupied, with a site energy ϵ_d which is large and negative and a large on-site Coulomb repulsion U. For definiteness, we assume that the nonmagnetic hybrid orbital is empty, with a site energy $\epsilon_h \approx 150$ meV which is far above the Fermi energy. The corresponding Hamiltonian takes the form

$$\begin{aligned} H = &\sum_{\mathbf{k}\sigma} \epsilon_{L\mathbf{k}} \psi^\dagger_{L\mathbf{k}\sigma} \psi_{L\mathbf{k}\sigma} + \sum_{\mathbf{k}\sigma} \epsilon_{R\mathbf{k}} \psi^\dagger_{R\mathbf{k}\sigma} \psi_{R\mathbf{k}\sigma} + \sum_\sigma \epsilon_h h^\dagger_\sigma h_\sigma + \sum_\sigma \epsilon_d d^\dagger_\sigma d_\sigma + U d^\dagger_\uparrow d^\dagger_\downarrow d_\downarrow d_\uparrow \\ &+ \sum_\sigma \Big[t_{Lh}(\mathbf{R}) h^\dagger_\sigma \psi_{L\sigma}(\mathbf{0}) + t_{Ld}(\mathbf{R}) d^\dagger_\sigma \psi_{L\sigma}(\mathbf{0}) + t_{Rh} \psi^\dagger_{R\sigma}(\mathbf{0}) h_\sigma + t_{Rd} \psi^\dagger_{R\sigma}(\mathbf{0}) d_\sigma + \text{h.c.} \Big] \end{aligned} \tag{S1}$$

Here, $\psi_\alpha(\mathbf{r}) = [\psi_{\alpha,\uparrow}(\mathbf{r}), \psi_{\alpha,\downarrow}(\mathbf{r})]^T$ is the spinor of electron field operators in the tip/substrate ($\alpha = L/R$) with Fourier transform $\psi_{\alpha\mathbf{k}\sigma}$. The operators $\psi_{L\sigma}(\mathbf{0})$ and $\psi_{R\sigma}(\mathbf{0})$ annihilate electrons in tip and substrate at the location of the tunnel junction to the molecular adsorbate. For the tip, the origin $\mathbf{0}$ is measured relative to a coordinate system attached to the tip.

The tunneling amplitude between tip and the two types of orbitals is denoted $t_{Lh}(\mathbf{R})$ and $t_{Ld}(\mathbf{R})$. These amplitudes depend sensitively on the position $\mathbf{R}$ of the tip, directly reflecting the wave functions of the respective orbital. In contrast, the tunnel couplings t_{Rh} and t_{Rd} are fully determined by the adsoption site of the adatom and thus independent of tip position.

Tunneling between tip and substrate will then proceed by cotunneling processes with virtual intermediate states, either a singly occupied nonmagnetic orbital or the empty and doubly occupied magnetic orbital. We can eliminate these virtual states by a Schrieffer-Wolff transformation and derive an effective low-energy Hamiltonian. The magnetic orbital introduces exchange and potential scattering terms,

$$H_d = \sum_{\alpha\alpha'} J^{(d)}_{\alpha\alpha'}(\mathbf{R}) \mathbf{S} \cdot \psi^\dagger_\alpha(\mathbf{0}) \boldsymbol{\sigma} \psi_{\alpha'}(\mathbf{0}) + \sum_{\alpha\alpha'} V^{(d)}_{\alpha\alpha'}(\mathbf{R}) \psi^\dagger_\alpha(\mathbf{0}) \psi_{\alpha'}(\mathbf{0}). \tag{S2}$$

Here, $\mathbf{S}$ denotes the impurity spin and $\boldsymbol{\sigma}$ is the vector of Pauli matrices. On the other hand, the nonmagnetic orbital contributes only a potential scattering term,

$$H_h = \sum_{\alpha\alpha'} V^{(h)}_{\alpha\alpha'}(\mathbf{R}) \psi^\dagger_\alpha(\mathbf{0}) \psi_{\alpha'}(\mathbf{0}). \tag{S3}$$

Explicitly, one obtains from the Schrieffer-Wolff transformation that

$$J^{(d)}_{\alpha\alpha'}(\mathbf{R}) = t_{\alpha d} t^*_{\alpha' d} \left[\frac{1}{\epsilon_d + U} - \frac{1}{\epsilon_d} \right] \quad ; \quad V^{(d)}_{\alpha\alpha'}(\mathbf{R}) = t_{\alpha d} t^*_{\alpha' d} \left[\frac{1}{\epsilon_d + U} + \frac{1}{\epsilon_d} \right] \tag{S4}$$

for virtual processes via the magnetic orbital, and

$$V^{(h)}_{\alpha\alpha'}(\mathbf{R}) = t_{\alpha h} t^*_{\alpha' h} \frac{1}{\epsilon_h} \tag{S5}$$

for processes via the nonmagnetic hybrid orbital.

We now use that the tunnel coupling between tip and orbital is much weaker than the orbital-substrate coupling. We can thus neglect processes which only involve the tip (i.e., $\alpha = \alpha' = L$) and account for the tunneling terms ($\alpha = L$ and $\alpha' = R$ or vice versa) perturbatively. Then, the adatom couples to the substrate through $J^{(d)}_{RR}$ and $V^{(d)}_{RR}$ as well as $V^{(h)}_{RR}$ in leading order. As we observe symmetric line shapes for tunneling directly into above the Fe atom, we assume that the magnetic orbital only leads to exchange coupling $J^{(d)}_{RR}$ and neglect the associated potential scattering $V^{(d)}_{RR}$ (as well as $V^{(d)}_{RL}$ and $V^{(d)}_{LR}$).

These considerations result in the effective Hamiltonian

$$H = H_0 + H_{\rm tun}. \tag{S6}$$

The unperturbed Hamiltonian

$$H_0 = \sum_{\mathbf{k}\sigma} \epsilon_{L\mathbf{k}} \psi^\dagger_{L\mathbf{k}\sigma} \psi_{L\mathbf{k}\sigma} + \sum_{\mathbf{k}\sigma} \epsilon_{R\mathbf{k}} \psi^\dagger_{R\mathbf{k}\sigma} \psi_{R\mathbf{k}\sigma} + J^{(\rm d)}_{RR}(\mathbf{R}) \mathbf{S} \cdot \psi^\dagger_R(\mathbf{0}) \boldsymbol{\sigma} \psi_R(\mathbf{0}). \tag{S7}$$

governs the interaction of the impurity spin with the substrate and also incorporates the Hamiltonian of the uncoupled tip. Tunneling from the tip introduces the perturbation

$$H_{\rm tun} = \psi^\dagger_R(\mathbf{0}) \left[J^{(\rm d)}_{RL}(\mathbf{R}) \mathbf{S} \cdot \boldsymbol{\sigma} + V^{(\rm h)}_{RL}(\mathbf{R}) \right] \psi_L(\mathbf{0}) + \text{h.c.}. \tag{S8}$$

It is now in principle a standard calculation to derive the current-voltage characteristic pertubatively in $H_{\rm tun}$ (Fermi's Golden Rule).

We remark that strictly speaking, this two-orbital model is not sufficient to describe our experimental system. Unlike in this model, in which $\mathbf{S}$ is a spin-1/2 impurity, Fe adatoms have a larger spin. This allows for single-ion anisotropy, which is not included in the Hamiltonian in Eq. (S6) and which underlies the spin excitations observed in the experiment. Single-ion anisotropy can be readily accounted for by adding $H_{\rm an} = DS_z^2 + E(S_x^2 - S_y^2)$ to Eq. (S6). In computing the currrent-voltage characteristics, it remains a nontrivial task to account for the exchange and potential scattering with the substrate (i.e., the terms with $\alpha = \alpha' = R$). When Kondo renormalizations are taken into account perturbatively, this task is performed by the program of Ternes [4].

Importantly, the tunneling rate and thus the current-voltage characteristics will include interference terms between the exchange scattering $J^{(\rm d)}_{RL}(\mathbf{R})$ originating from the magnetic orbital and the potential scattering $V^{(\rm h)}_{RL}(\mathbf{R})$ originating from the nonmagnetic orbital. The interference will be strongly dependent on the tip position $\mathbf{R}$. The exchange coupling $J^{(\rm d)}_{RL}(\mathbf{R})$ involves the tunneling amplitude t_{Ld} into the magnetic orbital, thus qualitatively following its spatial structure as a function of $\mathbf{R}$. In contrast, the potential scattering $V^{(\rm h)}_{RL}(\mathbf{R})$ involves the tunneling amplitude t_{Lh} into the nonmagnetic orbital, thus qualitatively following its spatial structure. The two tunneling amplitudes t_{Ld} and t_{Lh} govern the dependence on tip position $\mathbf{R}$ of (a) the relative importance of potential scattering (as parametrized through U at fixed J in the main paper) and (b) the overall tunneling strength.

[1] N. Krane, C. Lotze, and K. J. Franke, Surf. Sci. **678**, 136 (2018).
[2] J. Miwa, S. Ulstrup, S. G. Sørensen, M. Dendzik, A. Grubisić Cabo, M. Bianchi, J. V. Lauritsen, and P. Hofmann, Phys. Rev. Lett. **114**, 046802 (2014).
[3] A. Grubisić Cabo, J. A. Miwa, S. S. Grønborg, J. M. Riley, J. C. Johannsen, C. Cacho, O. Alexander, R. T. Chapman, E. Springate, M. Grioni, J. V. Lauritsen, P. D. C. King, P. Hofmann, and S. Ulstrup, Nano Lett. **15**, 5883 (2015).
[4] M. Ternes, New J. Phys. **17**, 063016 (2015).
[5] L. Farinacci, G. Ahmadi, M. Ruby, G. Reecht, B. W. Heinrich, C. Czekelius, F. von Oppen, and K. J. Franke, Phys. Rev. Lett. **125**, 256805 (2020).